Langmuir

Article

pubs.acs.org/Langmuir

Dynamic and Structural Properties of Room-Temperature Ionic Liquids near Silica and Carbon Surfaces

Song Li,[†] Kee Sung Han,[‡] Guang Feng,*[,†] Edward W. Hagaman,[‡] Lukas Vlcek,[‡] and Peter T. Cummings[†,§]

[†]Department of Chemical and Biomolecular Engineering, Vanderbilt University, Nashville, Tennessee 37235, United States

[‡]Chemical Sciences Division, and [§]Center for Nanophase Materials Sciences, Oak Ridge National Laboratory, Oak Ridge, Tennessee 37831, United States

Supporting Information

ABSTRACT: The dynamic and structural properties of a room-temperature ionic liquid (RTIL) 1-butyl-3-methyl-imidazolium-(trifluoromethanesulfonimide) ([C_4mim][Tf_2N]) confined in silica and carbon mesopores were investigated by molecular dynamics (MD) simulations and nuclear magnetic resonance (NMR) experiments. The complex interfacial microstructures of confined [C_4mim][Tf_2N] are attributed to the distinctive surface features of the silica mesopore. The temperature-dependent diffusion coefficients of [C_4mim][Tf_2N] confined in the silica or carbon mesopore exhibit divergent behavior. The loading fraction (f = 1.0, 0.5, and 0.25) has a large effect on the magnitude of the diffusion coefficient in the silica pore and displays weaker temperature dependence as the loading fraction decreases. The diffusion coefficients of mesoporous carbon-confined [C_4mim][Tf_2N] are relatively insensitive to the loading faction and exhibit a temperature dependence that is similar to the bulk dependence at all loading levels. Such phenomena can be attributed to the unique surface heterogeneity, dissimilar interfacial microstructures, and interaction potential profile of RTILs near silica and carbon walls.

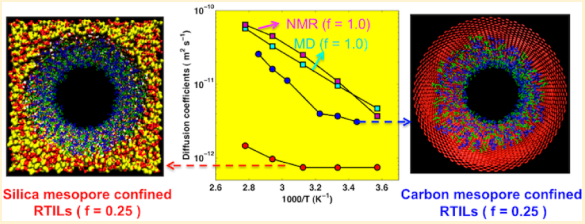

1. INTRODUCTION

Room-temperature ionic liquids (RTILs) are currently attracting widespread research interest because of a variety of properties (e.g., wide electrochemical window, low vapor pressure, non-flammability, and high conductivity)[1−3] and a wide range of applications (e.g., electrolytes,[4−6] lubricants,[7,8] and solvents[9]). Among these, the most attractive uses of RTILs are for energy-storage devices and lubricants. Both of these applications take advantage of the interfacial behavior of RTILs at solid−liquid interfaces. In energy-storage devices, such as supercapacitors, their performance is dominated by the electrical double layer (EDL), which is formed by the accumulated electrolytes near electrode surfaces.[10,11] The relationship between EDL microstructure and the energy stored has been investigated in a great number of studies.[12−17] The charging efficiency is determined by the solid−liquid interface as well.

Regardless of the ionic liquid itself, solid materials also play a vital role in determining the efficiency of charging/discharging of energy-storage devices. Both the constituent and surface properties of electrodes are responsible for the performance of energy-storage devices. At present, carbon- and silica-based materials are commonly used electrodes.[18,19] In comparison to molecularly smooth graphene-based carbons, such as graphene sheets and carbon nanotubes, the silica surface is mostly hydroxylated, thus generating nanoscale corrugation. Surface nanoroughness has been reported to retard the dynamics of liquids drastically.[20] Although a series of studies[21−23] of surface roughness effects on confined fluids has been reported, research on confined RTILs is incomplete. In the present work, the hydroxylated silica surface exhibits solvophilic-like properties in contrast to a solvophobic carbon surface. These terms are to be understood analogous to "hydrophilic" and "hydrophobic", respectively, used in the case where the solvent is water. Hence, a solvophilic surface can be easily solvated by polar solvents, while a solvophobic surface is not. The different behaviors of RTILs near solvophilic and solvophobic surfaces are critical for understanding the related application of RTILs in energy storage and lubrication.

RTILs were also reported to exhibit distinguishing properties under confinement compared to those in bulk.[24] The RTIL density near the interface is enhanced relative to the bulk and approaches the bulk value as the distance from the interface increases.[25,26] Therefore, the RTILs at the center of a mesopore were shown to exhibit a bulk-like dynamic behavior; in contrast, ions close to a solid surface displayed solid-like (rigid layer-by-layer) structure and slow dynamics. The restricted diffusion of confined RTILs has been investigated in numerous studies;[25−27] however, to our knowledge, the temperature effects on the dynamic properties of confined RTILs have not been

Received: March 27, 2013
Revised: June 11, 2013
Published: July 11, 2013

previously reported. The decrease of the melting temperature of RTILs was observed in the nanoporous silica matrix.[28,29] In a recent experimental study,[30] it was demonstrated that the compressed gas during RTIL loading dominated the variation of phase behavior; the loading of RTILs at high vacuum resulted in fully loaded nanopores with increased melting point and slower dynamics, and atmospheric loading resulted in partially filled nanopores with decreased melting point and enhanced dynamics. The effects of the loading fraction on structural and dynamic properties of RTILs were also investigated in a molecular dynamics (MD) simulation study.[27] Because of the vacuum environment of the mesopore in our simulation, samples with low RTIL loading fractions in the silica pore form a layer on the surface and their dynamics exhibit a loading fraction-dependent decrease. Therefore, understanding how the structure and dynamic properties of RTILs vary in relation to the method of confinement is essential for future applications in the areas of energy storage and lubrication relating to the solid−liquid region.

From the above-mentioned perspective, the fundamental study of the interfacial properties of RTILs near carbon and silica surfaces is of great interest. This work investigated the influence of different confinement environments on the dynamics and structural properties of 1-butyl-3-methyl-imidazolium(trifluoromethanesulfonimide) ($[C_4mim][Tf_2N]$) near solid−liquid interfaces (silica/$[C_4mim][Tf_2N]$ and carbon/$[C_4mim][Tf_2N]$) using MD simulations and nuclear magnetic resonance (NMR) measurements. The effects of the loading fraction and temperature were examined as well, which render the fundamental understanding of the interfacial behaviors of RTILs near different solid surfaces.

2. EXPERIMENTAL SECTION

2.1. Simulation Model and Setup. The amorphous silica was prepared by initially heating bulk silica up to 1800 K followed by gradually annealing to 300 K within 10 ns using MD package LAMMPS.[31] During this process, the ClayFF force field was adopted for bulk silica.[32] The silica mesopore with the diameter of 9.5 nm was carved in the bulk amorphous silica, and then simulation annealing was performed again for 10 ns. Afterward, the pore surface was fully hydroxylated at the experimental surface density of 4.6 OH/nm^2.[33] The hydroxylated silica pore was finally relaxed in a 200 ps MD simulation. The carbon mesopore was modeled by three layers of CNTs with a gap of 0.341 nm between each two neighboring layers. The inner tube has a diameter of 6.78 nm.

All production simulations in this work were performed using MD package GROMACS.[34] The exp-6 force field was used for RTIL $[C_4mim][Tf_2N]$.[35] All of the bonds were constrained during simulations. The time step of 1 fs was used to integrate the equation of motion with spherical cutoff of 1.1 nm in non-bonded van der Waals interactions. Long-range electrostatic interactions were treated by the particle mesh Ewald (PME) method.[36] Periodic boundary conditions were applied in three dimensions. The silica/carbon mesopore was completely frozen throughout the simulations, i.e., no movable atoms in silica/carbon mesopores. The force field for hydroxylated silica was adopted from ref 27. To obtain a reasonable density inside the pore at varying temperatures, grand canonical MD simulations were performed first using an isothermal−isobaric ensemble (NPT) at target temperatures (280, 300, 320, 340, and 360 K) and 1 bar. After equilibration, canonical (NVT) simulations were performed for $[C_4mim][Tf_2N]$-filled mesopores at different loading fractions (f = 1.0, 0.5, and 0.25) in the canonical ensemble. The simulation setup is shown in Figure 1.

The number of molecules in the fully filled pore was determined according to the grand canonical simulations. The different loading ratios were achieved by removing the proper amount of RTILs inside the fully filled pore to reach the specific volumetric ratio. After equilibration was completed for 8 ns, a 4−10 ns production run was generated. To investigate the temperature effects, the simulations were performed between 280 and 360 K with 20 K increments and 290, 300, 310, 330, 340, and 350 K for RTILs confined by carbon mesopores.

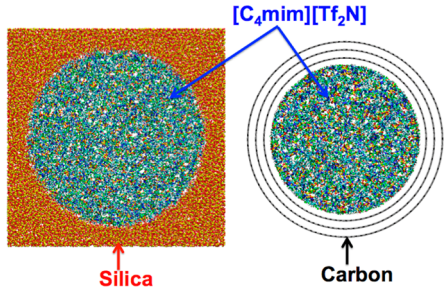

Figure 1. Cross-section view of the model silica and carbon mesopores filled with an ionic liquid.

The diffusion coefficient was calculated according to the Einstein relation.

$$D = \lim_{t\to\infty} \frac{1}{6t} \left\langle [r_i(t) - r_i(0)]^2 \right\rangle$$

After linear fitting of the mean square displacement (MSD), the diffusion coefficient was obtained from the fitted slope divided by 6. Note that, in simulations, the diffusion coefficient of C_4mim^+ ions was calculated to represent the diffusion property of $[C_4mim][Tf_2N]$ and compared to our experimental results, because NMR determined the diffusion of $[C_4mim][Tf_2N]$ based on the C_4mim^+ ions. For layer-by-layer diffusion, the confined RTILs $[C_4mim][Tf_2N]$ in silica/carbon are divided into five layers with the identical thickness along the radial direction. According to the initial location of the center of mass of ions, each ion is labeled with a layer number (1, 2, 3, 4, and 5). The MSD diffused by ions with a given layer number was calculated as a function of time. The diffusion coefficients of ions in individual layers were then obtained using the aforementioned method, because the radial diffusion of ions in the first two adsorbed layers is negligible and the other layers in bulk-like regions share similar dynamic properties.

The number density profiles were calculated along the radial direction of silica mesopores. The van der Waals and electrostatic interaction potentials for silica-confined $[C_4mim][Tf_2N]$ were calculated on the basis of the van der Waals equation and Coulomb's law, respectively. The cutoff distance was 1.1 nm. For carbon-confined $[C_4mim][Tf_2N]$, the Buckingham exp-6 potential was used to represent van der Waals interactions.

2.2. Materials Used in the Experiment. Mesoporous silica, KIT-6, having a 9.5 nm pore diameter, 783 m^2 g^{-1} surface area, and 1.11 cm^3 g^{-1} pore volume, was used in this work. The silica has a specific density of 1.43 g cm^{-3}. Using this characterization data, 227 mg of $[C_4mim][Tf_2N]$ is required to fill the pores of 144 mg of KIT-6. $[C_4mim][Tf_2N]$ was dissolved in 2 mL of ethanol, added to the silica, and stirred for 1 h. Ethanol was removed at 80 °C under weak vacuum for 24 h.

2.3. NMR Measurement. The diffusion coefficients of the C_4mim^+ cation in bulk and silica-confined $[C_4mim][Tf_2N]$ were measured by ^{1}H pulsed-field gradient (PFG) NMR[37] on a 9.4 T Bruker Avance 400 NMR spectrometer operating at a Larmor frequency of 400.1 MHz. The stimulated echo bipolar pulse-gradient pulse (stebpgp) sequence was used. The gradient strength was varied in 16 equal steps ranging from 2 to 95% of the maximum gradient strength of the probe, 54.4 ± 0.3 G cm^{-1}, which is determined by the ^{1}H magnetic resonance imaging method.[38] The echo height decay was fitted to the equation $S(g) = S(0)\exp[-D(\gamma\delta g)^2(\Delta - \delta/3)]$. Here, $S(g)$ and $S(0)$ are the echo heights at gradient strength g and 0, respectively. D is the diffusion coefficient; γ is the gyromagnetic ratio of ^{1}H; δ is the gradient-pulse length; and Δ is the duration between the two gradient pulses.[37]

dx.doi.org/10.1021/la401172z | Langmuir 2013, 29, 9744−9749

3. RESULTS AND DISCUSSION

As shown in Figure 1, the RTIL [C_4mim][Tf_2N] was confined in silica and carbon mesopores. The dynamics of confined [C_4mim][Tf_2N] were investigated over the temperature range from 280 to 360 K. Although the silica and carbon mesopore sizes in the model are different, the focus in this work is on the solid−liquid interfacial regions (silica/RTILs and carbon/RTILs) rather than the size effects. The diffusion coefficients of bulk and confined C_4mim^+ as a function of temperature at different loading fractions are shown in Figure 2. Clearly, once

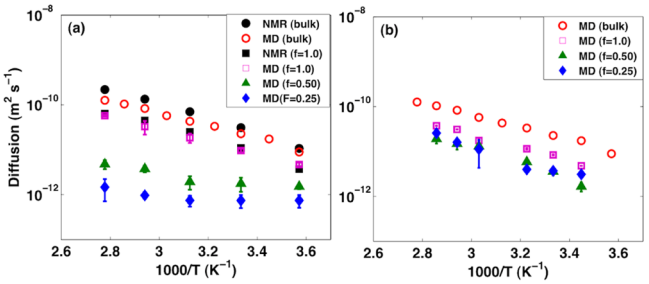

Figure 2. Diffusion coefficients of C_4mim^+ confined in (a) silica and (b) carbon mesopores as a function of temperature at different loading fractions (f).

confined, the diffusion of ions was slowed down in both mesopores, exhibiting similar trends seen in previous reports.[25−27] We also measured the diffusion properties of [C_4mim][Tf_2N] in bulk and confined in porous silica using the NMR technique. The trends obtained from NMR measurements are in good agreement with the MD results.

Moreover, as the loading fraction is decreased from 1.0 to 0.5 and then 0.25, the diffusion coefficients for silica-mesopore-confined [C_4mim][Tf_2N] declined dramatically. A similar trend was observed for carbon confinement as well, although the magnitude of the change is attenuated and is in accordance with previous studies.[27] Changes in the temperature cause different responses for silica and carbon mesopores. At low loading fractions, the temperature dependence of diffusion for silica-confined [C_4mim][Tf_2N] is weakened in comparison to that in carbon-confined [C_4mim][Tf_2N]. The diffusion coefficient of [C_4mim][Tf_2N] close to the silica surface is relatively insensitive to temperature variation. A similar change in slope is not observed for the temperature dependence of the diffusion coefficient as a function of the loading fraction in the carbon mesopore.

In contrast to translational diffusion, the rotational motion of C_4mim^+ in the silica pore at a low loading fraction exhibited significant temperature dependence, as shown in Figure S1 of the Supporting Information. The rotational correlation time of silica-confined C_4mim^+ increases as the loading fraction decreases and increases as the temperature declines.

The layer-by-layer analysis of the diffusion coefficients of [C_4mim][Tf_2N] in fully filled silica and carbon mesopores (Figure 3) revealed that ions in the central layers exhibit greater temperature dependence and higher diffusion coefficients compared to the layer closest to the silica walls (layer-1 in Figure 3a). In contrast, for [C_4mim][Tf_2N] confined in carbon, the ions exhibited similar temperature-dependent diffusion, regardless of the layer in which they were located. This suggests that the layer closest to the solid silica wall (i.e., layer-1 in Figure 3a) dominated the temperature dependence of diffusion

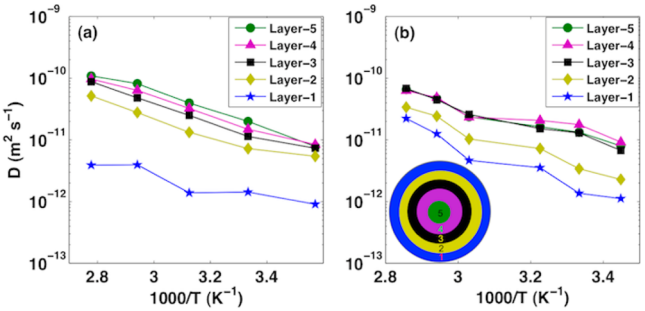

Figure 3. Layer-by-layer diffusion coefficients for (a) silica- and (b) carbon-mesopore-confined C_4mim^+ as a function of the temperature as predicted by MD simulation. The layer thickness is about 1.0 nm in panel a and 0.66 nm in panel b.

at low loading fractions, where the mobility of the ions was restricted. To further investigate the origins of the different temperature dependences of diffusion in confined [C_4mim][Tf_2N], the interfacial microstructures of [C_4mim][Tf_2N] in silica and carbon mesopores were calculated and shown in Figure 4.

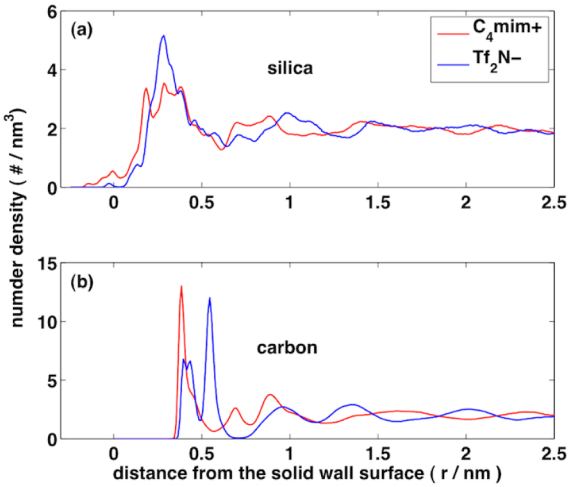

Figure 4. MD simulation result for the number density profile of [C_4mim][Tf_2N] (f = 1.0) confined in (a) silica and (b) carbon mesopores at 300 K.

Figure 4 displays the number density profiles of confined C_4mim^+ and Tf_2N^- as a function of the distance from the silica and carbon walls, respectively. The highest peak position for the cation and anion of silica-confined [C_4mim][Tf_2N] is approximately at 0.28 nm, which is closer to the solid walls compared to the peak position at 0.39 nm for cations and 0.56 nm for anions of carbon-confined [C_4mim][Tf_2N]. This is also true for partially loaded mesopores, as shown in Figure S2 of the Supporting Information, which displays the decreasing number of ion layers near the silica or carbon surfaces as the loading fraction is decreased. The first peak position is found to shift slightly toward the center of the pore as the loading fraction decreases, which is probably attributable to the increased fraction/mobility of ions located at ion/vacuum interfaces. According to the snapshots shown in the right panels of Figure S2 of the Supporting Information, as the loading fraction decreases, fewer ions are present inside pores, resulting in an increasingly inhomogeneous distribution across/on the pore. Compared to the carbon surface, the lower density near

dx.doi.org/10.1021/la401172z | Langmuir 2013, 29, 9744−9749

the silica surface is probably due to the limited accessible volume for ions, and the oscillation of the density profile near the silica surface is mainly due to the rough surface and non-uniform distribution of silica atoms. To describe the degree of surface roughness, the distribution of atoms as a function of the distance from the axis of silica or carbon mesopore was calculated and shown in Figure S3 of the Supporting Information. The atom number density in a silica mesopore gradually increases from 0 at 4.4 nm to the average density typical for the silica matrix. The non-uniform distribution of silica atoms indicates the surface roughness of the silica walls. In comparison to the heterogeneous silica surface, the carbon mesopores exhibit a constant number density located at three layers of the carbon mesopore, which is an indication of a smooth homogeneous carbon surface.

Furthermore, there is an obvious gap in the number density profile between ions and carbon wall. For the silica mesopore, there is more accessible space for ions (also see Figure 1); i.e., the ions penetrate into the small cavities in the surface driven by adsorption. This feature can be identified as solvophilic properties, which usually means that the solid wall has high affinity for solvents. In contrast, the carbon mesopore is considered as solvophobic, which repels $[C_4mim][Tf_2N]$ from its surface. The closer contact of water with a hydrophilic surface was observed in a recent simulation work.[39] It was also found that, in the vicinity of a rough surface, water molecules filled voids created by removed atoms.[40] Fuchs et al. investigated the structural properties of butane confined by smooth and corrugated walls with Monte Carlo simulations.[41] Their findings that the confined molecules are closer to a corrugated surface and the density near this surface is lower than near a smooth surface were also inspected in N_2 adsorption onto solid walls in another density functional theory (DFT) study.[40] The effects of roughness play a similar role as surface hydrophilicity or solvophilicity, which enables the closer contact of confined fluids and a wider range of density distributions compared to smooth hydrophobic/solvophobic surfaces. However, in our study, the degree of roughness of silica is not as remarkable as the nanoscale corrugation in the aforementioned studies.[39−41] The surface corrugations of silica can be mainly attributed to terminating surface hydroxyl groups that broaden the local disorder, which is in the sub-nanometer size. Therefore, roughness effects may not be the major cause of the different microstructures of RTILs near silica and carbon mesopores; solvophilicity of silica and solvophobicity of carbon might play a bigger role in forming different interfacial structures of RTILs. The force profiles on hydrophilic and hydrophobic spheres from AFM measurements displayed a jump near a hydrophobic surface,[42] which may be related to the gap in the number density profile for carbon mesopores. Nevertheless, whether such a difference is a result of the surface roughness or hydrophobicity is uncertain and may be a joint effect of both.

To explore the factors leading to distinctive structures of RTILs near silica and carbon surfaces, the interaction energy between ions and silica or carbon mesopore walls was calculated, as shown in Figure 5. Because of the atomic partial charges at silica surfaces, the electrostatic potential plays a role and dominates the interaction between ions and silica walls. The domination of the electrostatic interaction is evidenced by the number density profiles for the center of mass of the cation imidazolium ring and the carbon atom at the end of a cation alkyl chain shown in Figure S4 of the Supporting Information.

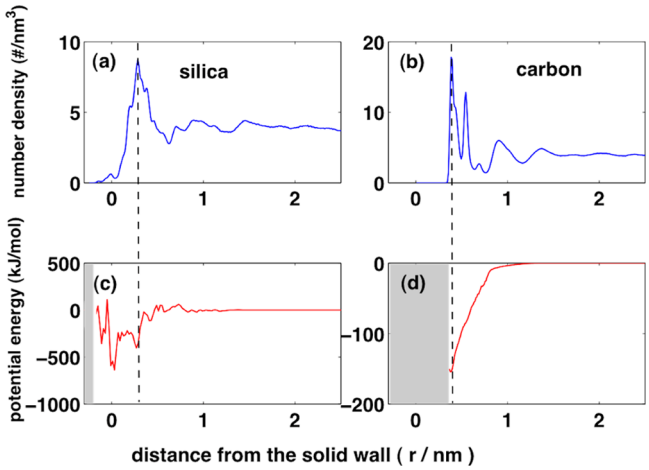

Figure 5. Total number density profile of $[C_4mim][Tf_2N]$ confined by (a) silica and (b) carbon mesopores and the averaged interaction potential per ion as a function of the distance toward the solid wall surface for (c) silica- and (d) carbon-confined $[C_4mim][Tf_2N]$ from MD simulations. The shaded areas in panels c and d represent the ion-free space.

For $[C_4mim][Tf_2N]$ in silica mesopore (see Figure S4a of the Supporting Information), the peak position for the highly positively charged ring is located at 0.33 nm, while the peak position shifts to 0.83 nm for the weakly charged alkyl tail. The difference of 0.5 nm approximates the distance from the center of the ring to the end of the carbon alkyl tail in one cation. On the contrary, the carbon-confined number density peak position for the ring nearly overlapped with that of the alkyl tail (see Figure S4b of the Supporting Information). This suggests that the electrostatic interaction drives the structuring near the silica walls and causes realignment of the cation ring and alkyl chains, which is not the case for $[C_4mim][Tf_2N]$ near carbon walls. It can be noted that alkyl chains diffuse deeper into the cavities in silica, which restrains the access of the relatively big cation rings. For carbon mesopores, in our MD simulations, only relatively weak van der Waals forces between ions and carbon walls contribute to the structuring of $[C_4mim][Tf_2N]$.

The peak in the number density profile corresponds to the negative attraction potential in the bottom panels of Figure 5. The dramatic fluctuation of the average interaction potential between ions and silica walls demonstrates the alternating attraction and repulsion occurring near the surface and contrasts with the unidirectional attraction near the carbon interface. For $r < 0$, the rugged surface features a large number of smaller and larger cavities with different electrostatic potentials, which may be more or less energetically favorable for different charged particles. While some of the cavities may be energetically favored, as indicated by the negative values of the potential, the entropic forces of confinement limit further penetration of fluid particles deeper into silica. It is worthwhile to note that, because the potential calculation is based on the binning method along the overall radial direction of the mesopore and the silica surface is not smooth, for the ions located in cavities that are below the average height of the surface, the binning direction is not normal to the local cavity surfaces. Therefore, there are apparent negative attraction peaks for cavity atoms beneath the silica surface observed in Figure 5c for $r < 0$. The fluctuating potential profile ($r > 0$) near the silica surface is analogous to the oscillatory force profile near hydrophilic surfaces measured in AFM experiments;[43] the less

dx.doi.org/10.1021/la401172z | Langmuir 2013, 29, 9744−9749

oscillatory force profile near the hydrophobic surface is observed as well in AFM measurements[43,44] and MD simulations.[44] Laria et al. observed the oscillating number density profile near hydrophilic and corrugated hydrophobic silica surfaces but less oscillating profile near the hydrophobic silica surface,[45] which agrees with our potential profile near silica and carbon walls. It may indicate that the experimentally observed oscillatory number density profile is determined by the interfacial potential profile.

Although the corresponding attractive potential for $[C_4mim][Tf_2N]$ in silica is larger in magnitude than that for $[C_4mim][Tf_2N]$ in carbon, it is noticed that the number density near silica is lower than that near the carbon surface. This probably can be attributed to the potential fluctuation in the silica−$[C_4mim][Tf_2N]$ interface; in contrast, the smoothly unidirectional potential profile facilitates the accumulation of ions near the carbon−$[C_4mim][Tf_2N]$ interface. However, even though the peak of the number density for silica-confined $[C_4mim][Tf_2N]$ is lower than that of carbon-confined $[C_4mim][Tf_2N]$, the total number of ions accumulated near the silica surface is higher than that near the carbon surface because of the increased accessible surface area of silica walls. Additionally, the number density for $r < 0.3$ nm might be underestimated, resulting from the inaccurate estimation of the volume close to silica walls because of the surface corrugation, which is not taken into account during the number density calculation. The potential profiles for cations and anions are shown in Figure S5 of the Supporting Information. Similar potential profiles for cations and anions near the carbon surface are present, whereas distinct profiles are disclosed for those near silica surfaces. The obvious attraction for cations and repulsion for anions around the silica surface ($r = 0$) lead to an increased number of cations and a decreased number of anions, as shown in the corresponding number density profiles, which, in another way, indicates the important influence of electrostatic potentials and surface roughness for silica pores.

It is known that surface heterogeneity and solvophobicity influence both the structural and dynamic properties of confined fluids near solid surfaces. Jun et al. reported on the reduced diffusion coefficients of confined particles in a rough channel using the numerical lattice Boltzmann method.[46] A similar behavior was reported in MD simulations as well.[23] Enhanced viscosity near a hydrophilic surface from MD simulation was reported by Netz et al.[39] Therefore, both surface roughness and hydrophilicity/solvophilicity can result in decreased diffusion. Although this behavior has been previously reported, the weakened temperature dependence of diffusion near a solvophilic and corrugated silica surface is reported here for the first time. It is reasonable to correlate the weakened temperature dependence of diffusion near solid walls with the surface heterogeneity and solvophilicity, which might facilitate the formation of layers directly in contact with solid walls with decreased temperature sensitivity. This rationalization of the weak temperature dependence of diffusion is still waiting to be verified experimentally.

4. CONCLUSION

In summary, this study reports the influence of different types of solid walls on the structural and dynamic properties of confined RTIL $[C_4mim][Tf_2N]$. The following phenomena were noted: (1) The diffusion coefficients of $[C_4mim][Tf_2N]$ confined in silica and carbon mesopores exhibited dissimilar temperature dependence as the loading fraction changed; (2) more complicated interfacial microstructures of $[C_4mim][Tf_2N]$ near solvophilic silica mesopores were observed; (3) an oscillatory interaction potential profile near the silica surface was revealed, in contrast to a non-oscillatory potential profile near a smooth carbon surface; and (4) both surface heterogeneity and features of the interaction potential for silica mesopores (i.e., electrostatic interaction) might contribute to the distinctive interfacial microstructure and weakened temperature dependence of diffusion. The closer contact of $[C_4mim][Tf_2N]$ with rough and solvophilic silica walls is in agreement with both theoretical and experimental reports. The observed oscillatory interaction potential profile near the silica surface coincides with the measured force profile from AFM measurements. The weakened temperature dependence of diffusion near silica surfaces at a low loading fraction is observed herein for the first time, which may be attributed to the surface roughness and solvophilicity. We hope that this study may inspire further experimental research on RTILs near differently featured solid walls as well as provide a baseline of neutral liquid−solid interfaces for the application of confined RTILs in the field of energy-storage devices.

■ ASSOCIATED CONTENT

Supporting Information

Rotational correlation time of cation C_4mim^+ as a function of the temperature for varying loading fractions in silica mesopores from MD simulation (Figure S1), number density profiles for cations and anions of $[C_4mim][Tf_2N]$ at 300 K near (a and c) silica and (b and d) carbon surfaces at loading ratios (a and b) $f = 0.25$ and (c and d) $f = 0.50$ (Figure S2), number density distribution of atoms in (a) silica and (b) carbon mesopores as a function of the distance from the pore axis from MD simulation (Figure S3), number density profile of the center of mass of the cation ring and the end carbon atom of the alkyl chain in the cation confined in (a) silica and (b) carbon mesopores from MD simulation (Figure S4), and number density profile of cations and anions of $[C_4mim][Tf_2N]$ confined by (a) silica and (b) carbon mesopores and the averaged interaction potential per ion as a function of the distance toward the solid wall surface for (c) silica- and (d) carbon-confined $[C_4mim][Tf_2N]$ from MD simulations (Figure S5). This material is available free of charge via the Internet at http://pubs.acs.org.

■ AUTHOR INFORMATION

Corresponding Author

*E-mail: guang.feng@vanderbilt.edu.

Notes

The authors declare no competing financial interest.

■ ACKNOWLEDGMENTS

This work was supported as part of the Fluid Interface Reactions, Structures, and Transport (FIRST) Center, an Energy Frontier Research Center funded by the Office of Basic Energy Sciences, Office of Science, U.S. Department of Energy. We acknowledge Oleg Borodin for graciously providing the exp-6 force field parameters used in this work. Computations for silica-confined ILs were performed on the Oak Ridge National Laboratory FIRST-funded cluster and at the National Energy Research Scientific Computing Center, which is supported by the Office of Science of the U.S. Department of Energy under Contract DE-AC02-05CH11231. Guang Feng

appreciates the Palmetto cluster at Clemson University for providing computer time.

REFERENCES

(1) Castner, E. W.; Wishart, J. F. Spotlight on ionic liquids. *J. Chem. Phys.* **2010**, 132.
(2) Weingaertner, H. Understanding ionic liquids at the molecular level: Facts, problems, and controversies. *Angew. Chem., Int. Ed.* **2008**, *47*, 654−670.
(3) Olivier, H. Recent developments in the use of non-aqueous ionic liquids for two-phase catalysis. *J. Mol. Catal. A: Chem.* **1999**, *146*, 285−289.
(4) Gorlov, M.; Kloo, L. Ionic liquid electrolytes for dye-sensitized solar cells. *Dalton Trans.* **2008**, 2655−2666.
(5) Devarajan, T.; Higashiya, S.; Dangler, C.; Rane-Fondacaro, M.; Snyder, J.; Haldar, P. Novel ionic liquid electrolyte for electrochemical double layer capacitors. *Electrochem. Commun.* **2009**, *11*, 680−683.
(6) Lee, J. S.; Bae, J. Y.; Lee, H.; Quan, N. D.; Kim, H. S.; Kim, H. Ionic liquids as electrolytes for Li ion batteries. *J. Ind. Eng. Chem.* **2004**, *10*, 1086−1089.
(7) Bermudez, M. D.; Jimenez, A. E.; Sanes, J.; Carrion, F. J. Ionic liquids as advanced lubricant fluids. *Molecules* **2009**, *14*, 2888−2908.
(8) Zhou, F.; Liang, Y. M.; Liu, W. M. Ionic liquid lubricants: Designed chemistry for engineering applications. *Chem. Soc. Rev.* **2009**, *38*, 2590−2599.
(9) Earle, M. J.; Seddon, K. R. Ionic liquids. Green solvents for the future. *Pure Appl. Chem.* **2000**, *72*, 1391−1398.
(10) Kornyshev, A. A. Double-layer in ionic liquids: Paradigm change? *J. Phys. Chem. B* **2007**, *111*, 5545−5557.
(11) Feng, G.; Zhang, J. S.; Qiao, R. Microstructure and capacitance of the electrical double layers at the interface of ionic liquids and planar electrodes. *J. Phys. Chem. C* **2009**, *113*, 4549−4559.
(12) Feng, G. A.; Qiao, R.; Huang, J. S.; Dai, S.; Sumpter, B. G.; Meunier, V. The importance of ion size and electrode curvature on electrical double layers in ionic liquids. *Phys. Chem. Chem. Phys.* **2011**, *13*, 1152−1161.
(13) Feng, G.; Huang, J. S.; Sumpter, B. G.; Meunier, V.; Qiao, R. A "counter-charge layer in generalized solvents" framework for electrical double layers in neat and hybrid ionic liquid electrolytes. *Phys. Chem. Chem. Phys.* **2011**, *13*, 14723−14734.
(14) Ania, C. O.; Pernak, J.; Stefaniak, F.; Raymundo-Pinero, E.; Beguin, F. Solvent-free ionic liquids as in situ probes for assessing the effect of ion size on the performance of electrical double layer capacitors. *Carbon* **2006**, *44*, 3126−3130.
(15) Lockett, V.; Sedev, R.; Ralston, J.; Horne, M.; Rodopoulos, T. Differential capacitance of the electrical double layer in imidazolium-based ionic liquids: Influence of potential, cation size, and temperature. *J. Phys. Chem. C* **2008**, *112*, 7486−7495.
(16) Shim, Y.; Kim, H. J. Nanoporous carbon supercapacitors in an ionic liquid: A computer simulation study. *ACS Nano* **2010**, *4*, 2345−2355.
(17) Bazant, M. Z.; Storey, B. D.; Kornyshev, A. A. Double layer in ionic liquids: Overscreening versus crowding. *Phys. Rev. Lett.* **2011**, 106.
(18) Frackowiak, E.; Beguin, F. Carbon materials for the electrochemical storage of energy in capacitors. *Carbon* **2001**, *39*, 937−950.
(19) Simon, P.; Gogotsi, Y. Materials for electrochemical capacitors. *Nat. Mater.* **2008**, *7*, 845−854.
(20) Ramiasa, M.; Ralston, J.; Fetzer, R.; Sedev, R. Nanoroughness impact on liquid−liquid displacement. *J. Phys. Chem. C* **2012**, *116*, 10934−10943.
(21) Xu, B. X.; Li, Y. B.; Park, T.; Chen, X. Effect of wall roughness on fluid transport resistance in nanopores. *J. Chem. Phys.* **2011**, 135.
(22) Sofos, F.; Karakasidis, T. E.; Liakopoulos, A. Effect of wall roughness on shear viscosity and diffusion in nanochannels. *Int. J. Heat Mass Transfer* **2010**, *53*, 3839−3846.
(23) Krekelberg, W. P.; Shen, V. K.; Errington, J. R.; Truskett, T. M. Impact of surface roughness on diffusion of confined fluids. *J. Chem. Phys.* **2011**, 135.
(24) Perkin, S. Ionic liquids in confined geometries. *Phys. Chem. Chem. Phys.* **2012**, *14*, 5052−5062.
(25) Monk, J.; Singh, R.; Hung, F. R. Effects of pore size and pore loading on the properties of ionic liquids confined inside nanoporous CMK-3 carbon materials. *J. Phys. Chem. C* **2011**, *115*, 3034−3042.
(26) Singh, R.; Monk, J.; Hung, F. R. A computational study of the behavior of the ionic liquid $[BMIM^+][PF_6^-]$ confined inside multiwalled carbon nanotubes. *J. Phys. Chem. C* **2010**, *114*, 15478−15485.
(27) Coasne, B.; Viau, L.; Vioux, A. Loading-controlled stiffening in nanoconfined ionic liquids. *J. Phys. Chem. Lett.* **2011**, *2*, 1150−1154.
(28) Singh, M. P.; Singh, R. K.; Chandra, S. Properties of ionic liquid confined in porous silica matrix. *ChemPhysChem* **2010**, *11*, 2036−2043.
(29) Kanakubo, M.; Hiejima, Y.; Minami, K.; Aizawa, T.; Nanjo, H. Melting point depression of ionic liquids confined in nanospaces. *Chem. Commun.* **2006**, 1828−1830.
(30) Chen, S. M.; Liu, Y. S.; Fu, H. Y.; He, Y. X.; Li, C.; Huang, W.; Jiang, Z.; Wu, G. Z. Unravelling the role of the compressed gas on melting point of liquid confined in nanospace. *J. Phys. Chem. Lett.* **2012**, *3*, 1052−1055.
(31) Plimpton, S. Fast parallel algorithms for short-range molecular dynamics. *J. Comput. Phys.* **1995**, *117*, 1−19.
(32) Cygan, R. T.; Liang, J. J.; Kalinichev, A. G. Molecular models of hydroxide, oxyhydroxide, and clay phases and the development of a general force field. *J. Phys. Chem. B* **2004**, *108*, 1255−1266.
(33) Zhuravlev, L. T. Concentration of hydroxyl groups on the surface of amorphous silicas. *Langmuir* **1987**, *3*, 316−318.
(34) Berendsen, H. J. C.; Vanderspoel, D.; Vandrunen, R. GROMACS: A message-passing parallel molecular-dynamics implementation. *Comput. Phys. Commun.* **1995**, *91*, 43−56.
(35) Borodin, O. Polarizable force field development and molecular dynamics simulations of ionic liquids. *J. Phys. Chem. B* **2009**, *113*, 11463−11478.
(36) Essmann, U.; Perera, L.; Berkowitz, M. L.; Darden, T.; Lee, H.; Pedersen, L. G.; Smooth, A. Particle mesh Ewald method. *J. Chem. Phys.* **1995**, *103*, 8577−8593.
(37) Johnson, C. S. Diffusion ordered nuclear magnetic resonance spectroscopy: Principles and applications. *Prog. Nucl. Magn. Reson. Spectrosc.* **1999**, *34*, 203−256.
(38) Yadav, N. N.; Torres, A. M.; Price, W. S. An improved approach to calibrating high magnetic field gradients for pulsed field gradient experiments. *J. Magn. Reson.* **2008**, *194*, 25−28.
(39) Sendner, C.; Horinek, D.; Bocquet, L.; Netz, R. R. Interfacial water at hydrophobic and hydrophilic surfaces: Slip, viscosity, and diffusion. *Langmuir* **2009**, *25*, 10768−10781.
(40) Yang, K.; Lin, Y. Z.; Lu, X. C.; Neimark, A. V. Solvation forces between molecularly rough surfaces. *J. Colloid Interface Sci.* **2011**, *362*, 382−388.
(41) Porcheron, F.; Schoen, M.; Fuchs, A. H. Monte Carlo simulation of a complex fluid confined to a pore with nanoscopically rough walls. *J. Chem. Phys.* **2002**, *116*, 5816−5824.
(42) Vinogradova, O. I.; Yakubov, G. E. Dynamic effects on force measurements. 2. Lubrication and the atomic force microscope. *Langmuir* **2003**, *19*, 1227−1234.
(43) Kaggwa, G. B.; Nalam, P. C.; Kilpatrick, J. I.; Spencer, N. D.; Jarvis, S. P. Impact of hydrophilic/hydrophobic surface chemistry on hydration forces in the absence of confinement. *Langmuir* **2012**, *28*, 6589−6594.
(44) Li, T. D.; Gao, J. P.; Szoszkiewicz, R.; Landman, U.; Riedo, E. Structured and viscous water in subnanometer gaps. *Phys. Rev. B: Condens. Matter Mater. Phys.* **2007**, *75*, 115415.
(45) Rodriguez, J.; Elola, M. D.; Laria, D. Confined polar mixtures within cylindrical nanocavities. *J. Phys. Chem. B* **2010**, *114*, 7900−7908.
(46) Jun, C.; Peng, X. F.; Lee, D. J. Diffusion coefficient of Brownian particle in rough micro-channel. *J. Colloid Interface Sci.* **2006**, *296*, 737−742.